SCIENCE CHINA
Technological Sciences

•Article•

January 2023 Vol.66 No.1: 223–232
https://doi.org/10.1007/s11431-022-2034-y

Design of protective and high sensitivity encapsulation layers in wearable devices

WANG XiuFeng[1*], HUANG JieLong[1], LIU YangChengYi[1], TAN JinYuan[1], CHEN ShangDa[1], AVILA Raudel[2] & XIE ZhaoQian[3*]

[1] *School of Materials Science and Engineering, Xiangtan University, Xiangtan 411105, China;*
[2] *Department of Mechanical Engineering, Northwestern University, Evanston, IL 60208, USA;*
[3] *State Key Laboratory of Structural Analysis for Industrial Equipment, Department of Engineering Mechanics, Dalian University of Technology, Dalian 116024, China*

Received January 8, 2022; accepted March 17, 2022; published online December 27, 2022

Elastomeric encapsulation layers are widely used in soft, wearable devices to physically isolate rigid electronic components from external environmental stimuli (e.g., stress) and facilitate device sterilization for reusability. In devices experiencing large deformations, the stress-isolation effect of the top encapsulation layer can eliminate the damage to the electronic components caused by external forces. However, for health monitoring and sensing applications, the strain-isolation effect of the bottom encapsulation layer can partially block the physiological signals of interest and degrade the measurement accuracy. Here, an analytic model is developed for the strain- and stress-isolation effects present in wearable devices with elastomeric encapsulation layers. The soft, elastomeric encapsulation layers and main electronic components layer are modeled as transversely isotropic-elastic mediums and the strain- and stress-isolation effects are described using isolation indexes. The analysis and results show that the isolation effects strongly depend on the thickness, density, and elastic modulus of both the elastomeric encapsulation layers and the main electronic component layer. These findings, combined with the flexible mechanics design strategies of wearable devices, provide new design guidelines for future wearable devices to protect them from external forces while capturing the relevant physiological signals underneath the skin.

strain-isolation effect, stress-isolation effect, elastomeric encapsulation, transversely isotropic medium, wearable devices

Citation: Wang X F, Huang J L, Liu Y C Y, et al. Design of protective and high sensitivity encapsulation layers in wearable devices. Sci China Tech Sci, 2023, 66: 223–232, https://doi.org/10.1007/s11431-022-2034-y

1 Introduction

Wearable electromechanical sensors transduce mechanical stimuli into readable electrical signals performing a similar function to that of human skin. Their functionality and ease of integration with the human body have positioned them as desirable candidates for potential applications in real-time health monitoring [1–4], human-machine interfaces [5,6], soft robotics [7,8], and neuroprosthetics [9,10]. At the skin-device interface, physiological processes like sweat, metabolites, and secretion create a complex operational environment for bare pressure sensors that degrade their performance. Therefore, a soft, elastomeric encapsulation layer with low water permeability is typically used to mitigate the effects of skin physiological processes in the device, such as chemical corrosion and device failure [11–15]. Further, the elastomeric encapsulation layer protects the pressure sensor from large mechanical deformations (so-called strain- and stress-isolation) [2,16,17] while in operation and facilitates assembly with other electronics components in the wearable device. Nevertheless, the effect of the encapsulation layer on the sensitivity of the pressure sensor

*Corresponding authors (email: onexf@xtu.edu.cn; zxie@dlut.edu.cn)

needs to be carefully studied [18] since a poor encapsulation design can cause a low signal-to-noise ratio and affect the capability to clearly distinguish between different subtle tactile signals (e.g., pulses and vocal vibrations) [12,19] in health monitoring applications.

Previous sophisticated encapsulation strategies reported in the literature, derived from elastic beam or shell model theories that include ultrasoft elastomers [20], elastomers with liquid-filled cavities [21], liquids surrounding hard electronic components [22] and electronic interconnects [23], aim to use the stress-isolation effect as a protective barrier for the electronics and sensors against large mechanical deformations (i.e., stretching) but the underlying mechanism degrading the sensitivity of the sensors, due to signal blocking, remains unclear. Motivated by this, an analytic model, based on the linear elasticity of the layers, is established to provide design strategies for wearable pressure sensors with a high sensitivity to distinguish the relevant physiological signals. The theoretical work presented here focuses on the strain- and stress-isolation effects of the elastomeric encapsulation layer, where analytical expressions for the stress and displacement distributions in the encapsulation layers are derived and validated by finite element analysis and three strategies are proposed for further optimization of multi-layer wearable systems.

2 Analytic model

Figure 1(a) shows a schematic exploded view of a wearable device interfaced with the skin (i.e., epidermal electronics), with an encapsulation strategy that relies on a three-layer system divided into a bottom (1st-layer) and top (3rd-layer) elastomeric layer that sandwiches the main electronic components layer (2nd-layer) to provide a strain- and stress-isolation effect, respectively. The stress-isolation (3rd-layer) protects the main electronic components layer (typically includes active sensors, the metallic serpentine-interconnects, microcontroller, and other peripheral passive components) from excessive stresses that could lead to metallic yield or fracture and maintains the measurement reliability during skin deformations. Conversely, the strain-isolation layer (1st-layer), weakens the initial physiological signal amplitude from the human epidermis affecting the measurement. The multi-layered wearable device can be modeled using the theory of the plane linear elastic problems in cylindrical coordinates, an analytic approach often used in the elastic analysis of multi-layered pavement structures [24–26]. Here, we consider the dynamic load (i.e., vibration signals) on the three-layer medium and focus on the stress/displacement distribution on the top/bottom surfaces of the main electronic components layer (2nd-layer). The top and bottom encapsulation layers are modeled as horizontal layered, homogeneous, and transversely isotropic solids. Assuming that the z-axis is perpendicular to the isotropic plane and the variables only depend on the radial and vertical directions (r and z), as shown in Figure 1(b). The governing equilibrium and constitutive equations for the axisymmetric problem can be written as follows.

(1) The stress equilibrium equations:

$$\frac{\partial \sigma_r}{\partial r}+\frac{\partial \tau_{zr}}{\partial z}+\frac{\sigma_r-\sigma_\theta}{r}=0, \tag{1a}$$

$$\frac{\partial \sigma_z}{\partial z}+\frac{\partial \tau_{zr}}{\partial r}+\frac{\tau_{zr}}{r}=\rho\frac{\partial^2 u_z}{\partial t^2}. \tag{1b}$$

(2) The constitutive equations:

$$\sigma_r=(\lambda+2G)\frac{\partial u_r}{\partial r}+\lambda\frac{u_r}{r}+\lambda\frac{\partial u_z}{\partial z}, \tag{2a}$$

$$\sigma_\theta=\lambda\frac{\partial u_r}{\partial r}+(\lambda+2G)\frac{u_r}{r}+\lambda\frac{\partial u_z}{\partial z}, \tag{2b}$$

$$\sigma_z=\lambda\left(\frac{\partial u_r}{\partial r}+\frac{u_r}{r}\right)+(\lambda+2G)\frac{\partial u_z}{\partial z}, \tag{2c}$$

$$\tau_{zr}=G\left(\frac{\partial u_r}{\partial z}+\frac{\partial u_z}{\partial r}\right), \tag{2d}$$

where E is Young's modulus, ρ is density and ν is Poisson's ratio, $\lambda=\frac{\nu E}{(1+\nu)(1-2\nu)}$ and $G=\frac{E}{2(1+\nu)}$ are the Lame constant and shear modulus, respectively. σ_r, σ_θ, σ_z, and τ_{zr} are the stress components in the cylindrical coordinate, and u_z is the displacement component. The set of equilibrium and constitutive equations is given in eqs. (1) and (2) coupling six partial differential equations to solve six unknowns. The

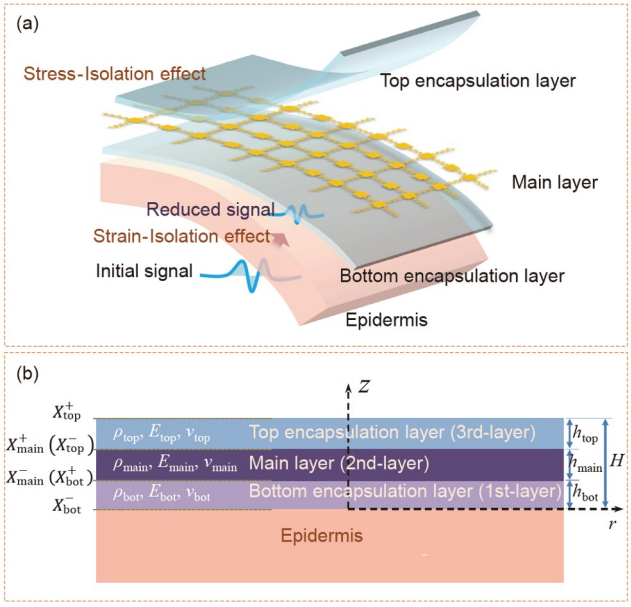

Figure 1 (Color online) (a) Illustration of a wearable device mounted on the epidermis, which consists of interconnects between islands of electrical components contained within a soft, elastomeric enclosure. (b) Axisymmetric schematic diagram of the encapsulated device modeled as a transversely isotropic three-layer medium.

state space formulation consists of describing physical phenomena in terms of the minimum possible number of variables. To achieve this, the first step is to reduce the number of state variables in eqs. (1) and (2) by eliminating the in-plane stress components σ_r and σ_θ, rendering a set of partial differential equations with four state variables as follows:

$$\begin{cases} \dfrac{\partial u_r}{\partial z} = -\dfrac{\partial u_z}{\partial r} + \dfrac{2(1+\nu)}{E}\tau_{zr}, \\ \dfrac{\partial u_z}{\partial z} = \dfrac{-\nu}{1-\nu}\left(\dfrac{\partial}{\partial r} + \dfrac{1}{r}\right)u_r + \dfrac{(1+\nu)(1-2\nu)}{E(1-\nu)}\sigma_z, \\ \dfrac{\partial \sigma_z}{\partial z} = \rho\dfrac{\partial^2 u_z}{\partial t^2} - \left(\dfrac{\partial}{\partial r} + \dfrac{1}{r}\right)\tau_{zr}, \\ \dfrac{\partial \tau_{zr}}{\partial z} = -\dfrac{E}{1-\nu^2}\left(\dfrac{\partial^2}{\partial r^2} + \dfrac{1}{r}\dfrac{\partial}{\partial r} - \dfrac{1}{r^2}\right)u_r + \dfrac{\nu}{1-\nu}\left(-\dfrac{\partial}{\partial r}\sigma_z\right). \end{cases} \tag{3}$$

Note that the displacement studied here exists in the time domain as an impulse function $u_z = u(r,z)e^{i\omega t}$, where ω is the angular frequency. Using the Hankel integral transform, all variables in eq. (3) can be transformed to depend only on ξ and z (Hankel transforms details are given in Appendix A in Supporting Information online), and eq. (3) can be reduced to a set of ordinary differential equations, which are rewritten simply in matrix form as

$$\frac{\mathrm{d}}{\mathrm{d}z}\tilde{\mathbf{X}}(\xi,z) = A(\xi)\tilde{\mathbf{X}}(\xi,z), \tag{4}$$

where

$$\tilde{\mathbf{X}}(\xi,z) = \left[\tilde{u}_r(\xi,z), \tilde{u}_z(\xi,z), \tilde{\sigma}_z(\xi,z), \tilde{\tau}_{zr}(\xi,z)\right]^{\mathrm{T}}, \tag{5a}$$

$$A(\xi) = \begin{bmatrix} 0 & \xi & 0 & \dfrac{2(1+\nu)}{E} \\ \dfrac{-\nu}{1-\nu}\xi & 0 & \dfrac{(1+\nu)(1-2\nu)}{E(1-\nu)} & 0 \\ 0 & -\rho\omega^2 & 0 & -\xi \\ \dfrac{E}{1-\nu^2}\xi^2 & 0 & \dfrac{\nu}{1-\nu}\xi & 0 \end{bmatrix}. \tag{5b}$$

The state vector solution in Hankel transform space for eq. (4) is expressed as (Details can be found in Appendix B):

$$\tilde{\mathbf{X}}(\xi,z) = C(\xi z)\tilde{\mathbf{X}}(\xi,0), \tag{6}$$

where $C(\xi z)$ is the transfer matrix between the initial state vector $\tilde{\mathbf{X}}(\xi,0)$ and the state vector $\tilde{\mathbf{X}}(\xi,z)$ of arbitrary depth z. By analyzing the eigenvalues of $A(\xi)$ in eq. (5b), the components of the transfer matrix $C(\xi z)$ can be derived as [27]

$$C_{11} = \mathrm{Ch}z\xi - \frac{z\xi \mathrm{Sh}z\xi}{2(\nu-1)},\ C_{12} = \frac{z\xi[(1+\nu)\eta^2-\xi^2]\mathrm{Ch}z\xi - [(1+\nu)\eta^2+(1-2\nu)\xi^2]\mathrm{Sh}z\xi}{2(\nu-1)\xi^2},$$

$$C_{13} = -\frac{(1+\nu)z\mathrm{Sh}z\xi}{2E(\nu-1)},\ C_{14} = \frac{(1+\nu)(-z\xi\mathrm{Ch}z\xi+(4\nu-3)\mathrm{Sh}z\xi)}{2E(\nu-1)\xi},$$

$$C_{21} = \frac{z\xi\left[(\nu-\nu^2-2\nu^3)\eta^2+(\nu-1)\xi^2\right]\mathrm{Ch}z\xi+(2\nu-1)\left[(\nu+\nu^2)\eta^2+(\nu-1)\xi^2\right]\mathrm{Sh}z\xi}{2(\nu-1)^2\xi^2},\ C_{22} = \mathrm{Ch}z\xi + \frac{z\left[(1-\nu-2\nu^2)\eta^2+\xi^2\right]\mathrm{Sh}z\xi}{2(-1+\nu)\xi},$$

$$C_{23} = (1+\nu)\frac{z\xi\left[(\nu-1)\xi^2-(1-3\nu+4\nu^3)\eta^2\right]\mathrm{Ch}z\xi+\left[(1-3\nu+4\nu^3)\eta^2+(3-7\nu+4\nu^2)\xi^2\right]\mathrm{Sh}z\xi}{2E(\nu-1)^2\xi^3},$$

$$C_{24} = \frac{(1+\nu)z\mathrm{Sh}z\xi}{2E(\nu-1)},\ C_{31} = -\frac{Ez\left[(\nu+\nu^2)\eta^2-\xi^2\right]\mathrm{Sh}z\xi}{2(\nu^2-1)},$$

$$C_{32} = \frac{Ez\xi\left[(2\nu^3+3\nu^2-1)\eta^4-(1+\nu)^2\eta^2\xi^2+\xi^4\right]\mathrm{Ch}z\xi+\left[(1-3\nu^2-2\nu^3)\eta^4+(3+2\nu-\nu^2)\eta^2\xi^2-\xi^4\right]\mathrm{Sh}z\xi}{2(\nu^2-1)\xi^3},\ C_{33} = C_{22},\ C_{34} = -C_{12},$$

$$C_{41} = \frac{zE\xi\left[(\nu^2+\nu^3)\eta^2-(\nu-1)\xi^2\right]\mathrm{Ch}z\xi-\left[(\nu^2+\nu^3)\eta^2+(\nu-1)\xi^2\right]\mathrm{Sh}z\xi}{2(\nu-1)^2(1+\nu)\xi},\ C_{42} = -C_{31},\ C_{43} = -C_{21},\ C_{44} = C_{11}, \tag{7a}$$

where $\eta = \omega\sqrt{\rho/E}$ is a vibration parameter. When the vibration disappears ($\omega \to 0$) and produces $\eta \to 0$, the transfer matrix $\mathbf{C}(\xi z)$ can be simplified as

$$\mathbf{C}(\xi z) = \begin{bmatrix} \mathrm{ch}\xi z + \dfrac{z\xi\mathrm{sh}\xi z}{2(1-\nu)} & \dfrac{(1-2\nu)\mathrm{sh}\xi z + z\xi\mathrm{ch}\xi z}{2(1-\nu)} & \dfrac{(1+\nu)z\mathrm{sh}\xi z}{2E(1-\nu)} & \dfrac{(1+\nu)(z\xi\mathrm{ch}\xi z+(3-4\nu)\mathrm{sh}\xi z)}{2E(1-\nu)\xi} \\ \dfrac{(1-2\nu)\mathrm{sh}\xi z - z\xi\mathrm{ch}\xi z}{2(1-\nu)} & \mathrm{ch}\xi z - \dfrac{z\xi\mathrm{sh}\xi z}{2(1-\nu)} & \dfrac{(1+\nu)(z\xi\mathrm{ch}\xi z+(3-4\nu)\mathrm{sh}\xi z)}{2E(1-\nu)\xi} & \dfrac{(1+\nu)z\mathrm{sh}\xi z}{2E(1-\nu)} \\ -\dfrac{Ez\xi^2\mathrm{sh}\xi z}{2(1-\nu^2)} & \dfrac{\xi E(\mathrm{sh}\xi z - z\xi\mathrm{ch}\xi z)}{2(1-\nu^2)} & \mathrm{ch}\xi z - \dfrac{z\xi\mathrm{sh}\xi z}{2(1-\nu)} & -\dfrac{z\xi\mathrm{ch}\xi z+(1-2\nu)\mathrm{sh}\xi z}{2(1-\nu)} \\ \dfrac{\xi E(\mathrm{sh}\xi z + z\xi\mathrm{ch}\xi z)}{2(1-\nu^2)} & \dfrac{Ez\xi^2\mathrm{sh}\xi z}{2(1-\nu^2)} & \dfrac{z\xi\mathrm{ch}\xi z-(1-2\nu)\mathrm{sh}\xi z}{2(1-\nu)} & \mathrm{ch}\xi z + \dfrac{z\xi\mathrm{sh}\xi z}{2(1-\nu)} \end{bmatrix}. \tag{7b}$$

For the encapsulated device shown in Figure 1, the h_i, ρ_i, G_i, E_i and v_i represent the thickness, density, shear modulus, Young's modulus, and the Poisson ratio of the ith layer, where the label i = top, main, or bot, represents the top encapsulation layer, the main layer, and the bottom encapsulation layer, respectively. The vibration parameter can be rewritten as $\eta_i = \omega\sqrt{\rho_i / E_i}$. The total thickness of the device is $H = h_{\text{top}} + h_{\text{main}} + h_{\text{bot}}$, and the state vector at the top surface (or bottom surface) of the ith layers is labeled as $\widetilde{\mathbf{X}}_i^+$ (or $\widetilde{\mathbf{X}}_i^-$) as shown in Figure 1(b). By using eq. (6) the transfer relations between the state vector at the top and bottom surfaces of the ith layer can be expressed as

$$\widetilde{\mathbf{X}}_i^+(\xi, h_i) = C_i(\xi h_i, \eta_i, G_i, v_i)\widetilde{\mathbf{X}}_i^-(\xi, 0), \tag{8}$$

and the continuity conditions at the layer interfaces are given as

$$\begin{cases} \widetilde{\mathbf{X}}_{\text{bot}}^+(\xi, h_{\text{bot}}) = \widetilde{\mathbf{X}}_{\text{main}}^-(\xi, 0), \\ \widetilde{\mathbf{X}}_{\text{main}}^+(\xi, h_{\text{main}}) = \widetilde{\mathbf{X}}_{\text{top}}^-(\xi, 0). \end{cases} \tag{9}$$

Using eqs. (8) and (9), the state vector at the interfaces can be eliminated, and the transfer relations between $\widetilde{\mathbf{X}}_{\text{top}}^+(\xi, H)$ at the top encapsulation layer and $\widetilde{\mathbf{X}}_{\text{bot}}^-(\xi, 0)$ at the bottom encapsulation layer can be expressed as

$$\widetilde{\mathbf{X}}_{\text{top}}^+(\xi, H) = C_{\text{top}}C_{\text{main}}C_{\text{bot}}\widetilde{\mathbf{X}}_{\text{bot}}^-(\xi, 0). \tag{10a}$$

Applying the boundary conditions at the top and bottom encapsulation layers, the concerned state vector at the top and bottom surfaces of the main layer can be further obtained as

$$\widetilde{\mathbf{X}}_{\text{main}}^-(\xi, h_{\text{bot}}) = C_{\text{bot}}\widetilde{\mathbf{X}}_{\text{bot}}^-(\xi, 0), \tag{10b}$$

$$\widetilde{\mathbf{X}}_{\text{main}}^+(\xi, H - h_{\text{top}}) = C_{\text{top}}\widetilde{\mathbf{X}}_{\text{top}}^+(\xi, H), \tag{10c}$$

where $C_i(\xi h_i)$ is the transfer matrix of the ith layer (Figure 1 (b)).

3 Results and discussion

The effect of the layered encapsulated medium on the main layer of the device (where passive/active electronic components and serpentine interconnects reside) is discussed based on the theoretical framework for layered isotropic elastic solids presented in the previous section. Here, two different loading modes were investigated. The first is the decay of the internal physiological signal originating from the epidermis traveling through the bottom encapsulation layer until it reaches the bottom surface of the main layer; this loading mode is defined as the strain-isolation effect or SAI. The second is the maximum stress generated on the top surface of the main layer due to external loading above the top encapsulation layer that can damage the internal serpentine interconnects and/or electronic components; this loading mode is defined as the stress-isolation effect or SEI.

3.1 Strain-isolation effect on internal physiological signal.

Recently reported wearable devices mounted on the skin can detect various physiological signals, including respiration [28,29], pulse [30,31], heartbeat [7,32], and fetal movement [33] (examples of physiological parameters are listed in Table 1), among others. For convenience, a simplified mathematical form to describe these complex vibration signals is adopted as

$$u_z(r,z)\big|_{z=0} = u_z(r,0) = u_0 \mathrm{e}^{\mathrm{i}\omega t - Rr^2}, \tag{11}$$

where u_0, ω and R are the amplitude (from dozens of micrometers to several millimeters), the angular frequencies (from 0.1 to 2 Hz) and the vibration range of the physiological signals (from several millimeters to several decimeters), respectively.

The original physiological signal $u_z(r,0)$ is transmitted to the pressure sensor after passing through the strain-isolation (bottom or 1st) layer, and the decayed signal $u_z(r,z)\big|_{z=h_{\text{bot}}} = u_z(r, h_{\text{bot}})$ must be determinated (Figure 2 (a)–(i)). Considering a traction-free condition on top surface of the top encapsulation layer, the boundary conditions of the system are written as follows:

$$\begin{cases} u_r(r,z)\big|_{z=0} = 0, \\ u_z(r,z)\big|_{z=0} = u_0 \mathrm{e}^{\mathrm{i}\omega t - Rr^2} (|r| \leqslant R), \\ \sigma_z(r,z)\big|_{z=H} = 0, \\ \tau_{zr}(r,z)\big|_{z=H} = 0. \end{cases} \tag{12a}$$

Using the Hankel transform in eq. (S1a), the following is obtained:

$$\begin{cases} \tilde{u}_r(\xi,z)\big|_{z=0} = 0, \\ \tilde{u}_z(\xi,z)\big|_{z=0} = u_0 \int_0^\infty \mathrm{e}^{\mathrm{i}\omega t - Rr^2} r J_0(\xi r)\mathrm{d}r = \dfrac{u_0}{2R}\mathrm{e}^{\mathrm{i}\omega t - \frac{\xi^2}{4R}}, \\ \tilde{\sigma}_z(\xi,z)\big|_{z=H} = 0, \\ \tilde{\tau}_{zr}(\xi,z)\big|_{z=H} = 0. \end{cases} \tag{12b}$$

Substituting eq. (12b) into eq. (10a) gives

Table 1 Mechanical and thermal properties of the specimens

	Frequency ω (min^{-1})	Range R (mm)
Pulse	60–100	2–5
Heartbeat	60–100	15–25
Respiration	12–20	40–60

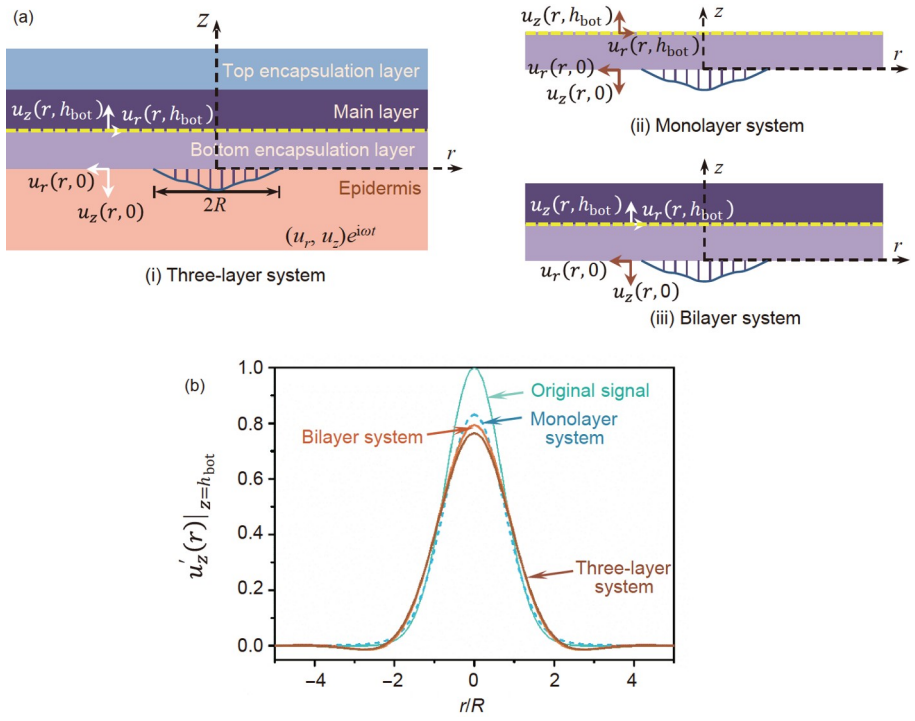

Figure 2 (Color online) (a) Schematic illustration of strain-isolation effect in encapsulation systems with different layers. (b) Distribution of $u_z^{'}(r)$ at the bottom surface of the main layer for different systems.

$$\begin{pmatrix} \tilde{u}_r(\xi,z)\big|_{z=H} \\ \tilde{u}_z(\xi,z)\big|_{z=H} \\ 0 \\ 0 \end{pmatrix} = C(\xi)\begin{pmatrix} 0 \\ \dfrac{u_0}{2R}\mathrm{e}^{\mathrm{i}\omega t-\frac{\xi^2}{4R}} \\ \tilde{\sigma}_z(\xi,z)\big|_{z=0} \\ \tilde{\tau}_{zr}(\xi,z)\big|_{z=0} \end{pmatrix}, \tag{13}$$

where $C(\xi)=C_{\mathrm{top}}\left(\xi h_{\mathrm{top}}\right)C_{\mathrm{main}}\left(\xi h_{\mathrm{main}}\right)C_{\mathrm{bot}}\left(\xi h_{\mathrm{bot}}\right)$. Solving eq. (13), the stress components are obtained as

$$\begin{cases} \tilde{\sigma}_z(\xi,z)\big|_{z=0} = \dfrac{u_0}{2R}\dfrac{(C_{32}C_{44}-C_{34}C_{42})}{C_{34}C_{43}-C_{33}C_{44}}\mathrm{e}^{\mathrm{i}\omega t-\frac{\xi^2}{4R}}, \\ \tilde{\tau}_{zr}(\xi,z)\big|_{z=0} = \dfrac{u_0}{2R}\dfrac{(C_{33}C_{42}-C_{32}C_{43})}{C_{34}C_{43}-C_{33}C_{44}}\mathrm{e}^{\mathrm{i}\omega t-\frac{\xi^2}{4R}}, \end{cases} \tag{14}$$

where $C_{ij}(i,j=1,2,3\text{ and }4)$ are the elements of matrix $C(\xi)$. Based on eq. (13) and eq. (10b), the state vector at the interface between the sensor and bottom encapsulation layer is governed by

$$\mathbf{X}_{\mathrm{main}}^{-}\left(\xi,h_{\mathrm{bot}}\right)=\begin{pmatrix} \tilde{u}_r(\xi,z)\big|_{z=h_{\mathrm{bot}}} \\ \tilde{u}_z(\xi,z)\big|_{z=h_{\mathrm{bot}}} \\ \tilde{\sigma}_z(\xi,z)\big|_{z=h_{\mathrm{bot}}} \\ \tilde{\tau}_{zr}(\xi,z)\big|_{z=h_{\mathrm{bot}}} \end{pmatrix} = \mathbf{C}_{\mathrm{bot}}\left(\xi h_{\mathrm{bot}}\right)\begin{pmatrix} 0 \\ \dfrac{u_0}{2R}\mathrm{e}^{\mathrm{i}\omega t-\frac{\xi^2}{4R}} \\ \tilde{\sigma}_z(\xi,z)\big|_{z=0} \\ \tilde{\tau}_{zr}(\xi,z)\big|_{z=0} \end{pmatrix}. \tag{15}$$

Solving the eq. (15), the vertical displacement $\tilde{u}_z(\xi,z)$ at the bottom layer is obtained as

$$\begin{aligned} \tilde{u}_z(\xi,z)\big|_{z=h_{\mathrm{bot}}} &= A_{22}\frac{u_0}{2R}\mathrm{e}^{\mathrm{i}\omega t-\frac{\xi^2}{4R}}+A_{23}\tilde{\sigma}_z(\xi,z)\big|_{z=0} \\ &\quad +A_{24}\tilde{\tau}_{zr}(\xi,z)\big|_{z=0}, \end{aligned} \tag{16a}$$

where $A_{ij}(i,j=1,2,3\text{ and }4)$ are the elements of matrix $C_{\mathrm{bot}}\left(\xi h_{\mathrm{bot}}\right)$. Substituting eq. (14) into eq. (16a) and using the Hankel inverse transform in eq. (S1b), the normalized displacement component at the interface between the sensor and bottom encapsulation layer is obtained:

$$\begin{aligned} u_z^{'}(r,z)\big|_{z=h_{\mathrm{bot}}} &= \left.\frac{u_z(r,z)}{u_0\mathrm{e}^{\mathrm{i}\omega t}}\right|_{z=h_{\mathrm{bot}}} \\ &= \left.\frac{1}{u_0\mathrm{e}^{\mathrm{i}\omega t}}\int_0^{\infty}\tilde{u}_z(\xi,z)\,\xi\,J_0(\xi r)\mathrm{d}\xi\right|_{z=h_{\mathrm{bot}}}, \end{aligned} \tag{16b}$$

where $J_0(\xi)$ is the zero order Bessel function. To evaluate the degree of signal decay in the bottom encapsulation layer, a strain-isolation index κ_1 is introduced to define the original signal decrease from the maximum amplitude as

$$\begin{aligned} \kappa_1 &= 1-\mathrm{Max}\left[u_z^{'}(\xi,z)\big|_{z=h_{\mathrm{bot}}}\right] \\ &= 1-\left.\frac{1}{u_0\mathrm{e}^{\mathrm{i}\omega t}}\int_0^{\infty}\tilde{u}_z(\xi,z)\,\xi\,J_0(\xi r)\mathrm{d}\xi\right|_{r=0,z=h_{\mathrm{bot}}}. \end{aligned} \tag{17}$$

If the vibration is weak ($\omega\to 0$) and three-layer homogeneous media take the same elastic modulus ($E_{\mathrm{top}}=E_{\mathrm{main}}=E_{\mathrm{bot}}=E$, $\nu_{\mathrm{top}}=\nu_{\mathrm{main}}=\nu_{\mathrm{bot}}=\nu$), the solution in eq. (13) degenerates to

$$\begin{cases}\tilde{\sigma}_z(\xi,z)\big|_{z=0} = \dfrac{E}{R(1+\nu)}\dfrac{(1-\nu)[2H\xi-\sinh(2H\xi)]}{b+c\cosh(2H\xi)}\xi u_0 e^{i\omega t-\frac{\xi^2}{4R}},\\ \tilde{\tau}_{zr}(\xi,z)\big|_{z=0} = \dfrac{E}{2R(1+\nu)}\dfrac{(1-2\nu)[1-\cosh(2H\xi)]-2H^2\xi^2}{b+c\cosh(2H\xi)}\xi u_0 e^{i\omega t-\frac{\xi^2}{4R}},\\ \tilde{u}_r(\xi,z)\big|_{z=H} = \dfrac{2(1-\nu)}{R}\dfrac{H\xi\cosh(H\xi)+(1-2\nu)\sinh(H\xi)}{b+c\cosh(2H\xi)}u_0 e^{i\omega t-\frac{\xi^2}{4R}},\\ \tilde{u}_z(\xi,z)\big|_{z=H} = \dfrac{2(1-\nu)}{R}\dfrac{H\xi\sinh(H\xi)+2(1-\nu)\cosh(H\xi)}{b+c\cosh(2H\xi)}u_0 e^{i\omega t-\frac{\xi^2}{4R}}.\end{cases}$$

And $\tilde{u}_z(\xi,z)$ in eq. (17) for calculating the strain-isolation index becomes

$$\tilde{u}_z(\xi,z)\big|_{z=h_{bot}} = \frac{u_0}{2R}\frac{c[\cosh(a\xi)+\xi a\sinh(z\xi)]+(b-2zH\xi^2)\cosh(z\xi)+\xi z\sinh(a\xi)}{b+c\cosh(2H\xi)}e^{i\omega t-\frac{\xi^2}{4R}}, \tag{18}$$

where $a = 2H-z$, $b = 5-12\nu+8\nu^2+2H^2\xi^2$, and $c = 3-4\nu$. For the special case of a monolayer system with $H = h_{bot}$ (Figure 2(a)-ii), the strain-isolation index can be further simplified to

$$\kappa_1 = 1-\frac{2(1-\nu)}{R}\int_0^{\infty}\frac{H\xi\sinh(H\xi)+2(1-\nu)\cosh(H\xi)}{5-12\nu+8\nu^2+2H^2\xi^2+(3-4\nu)\cosh(2H\xi)}e^{-\frac{\xi^2}{4R}}\xi J_0(\xi r)\mathrm{d}\xi\Big|_{r=0}. \tag{19}$$

Eqs. (16a) and (17) predict the normalized displacement components of the vibration signal at the top of the encapsulation layer and evaluate the strain-isolation effect of the device after encapsulation. It is noted that eqs. (18) and (19) can be adopted as the lower limit for evaluating the strain-isolation effect of the bottom encapsulation layer.

Figure 2(b) shows the distribution of the signal $u_z'(r)\big|_{z=h_{bot}}$ for three systems with different layers. The strain-isolation effects are larger for a multi-layered system as the number of layers increases where the monolayer system exhibits the lower SAI limit obtained from eq. (19). Figure 3(a) shows the signal $u_z'(r)\big|_{z=h_{bot}}$ of a three-layer system versus r/R for $\eta_{bot}R = \eta_{top}R = \eta_{main}R/10 = 0.001$, $E_{bot} = E_{top} = E_{main}/10$, $\nu = 0.5$, $h_{main} = h_{top} = R/2$ and $h_{bot}/R = 0.25$, 0.5, 0.75, 1 (example of soft elastomeric enclosures typically used in wearable devices are listed in Table 2). The results indicate that half of the signal amplitude would be shielded by the bottom encapsulation layer when its thickness h_{bot} is comparable to equivalent to the signal range, R. To identify the effect of each layer in the SAI via the strain-isolation index κ_1, the thickness of an individual layer was changed by the ratio $h_i/R = 0.25$, 0.5, 0.75, 1 (i=top, main, bot) while the thickness of the remaining two layers was fixed to $h_i/R = 0.5$. The results in Figure 3(b) indicate that the bottom encapsulation layer has the most significant effect on the SAI as the κ_1 varies from 5% to 50% when the bottom layer thickness changes. For the main layer, the effect on the SAI is reduced, as shown by the changes between 14% and 35% in the κ_1 and the top encapsulation layer shows a relatively small effect on the SAI as the variation in the κ_1 is almost negligible when the top layer thickness changes.

In addition to the thickness of the elastomeric layers, the density, vibration frequency and elastic modulus of each layer also affect the SAI, which can be combined into a single parameter $\eta = \omega\sqrt{\rho/E}$ (mentioned in Sect. 2). Figure 3(c) shows κ_1 versus $\eta_{top}R$ for a three-layer system with different Young's modulus ratios between the main and top encapsulation layers (E_{main}/E_{bot} = 1, 10, 100, and 1000) for a device with a fixed thickness ($h_{top} = h_{main} = h_{bot} = R/4$). The results show that the strain-isolation effect can be reduced by increasing the density of the 1st-layer, and even further relieved by decreasing the modulus of the 2nd-layer, i.e., adopting encapsulating materials with a high density and the layout of electronic components with low effective elastic modulus. For the case when the main layer is very rigid as compared to the top encapsulation layer by several orders of magnitude (e.g., $E_{main}/E_{bot} = 10^7$), the strain-isolation effect becomes very strong and κ_1 approaches 1, i.e., 100% of the original signal is lost (Figure 3(d)). Recently, researchers adopted air- or Silicon gel-pocket layout to enclose the main layer (2nd-layer), which allows free movement of the serpentine interconnects and islands of components, then obtained the main layers with ultra-low equivalent modulus [32,34–38]. These designs leave the sensors in conformal contact with skin and greatly alleviate the strain-isolation effect (SAI). Previous works demonstrate that the effective Young's moduli of the layout of the main layer would be optimized as low as that of encapsulating layer ($E_{bot}/E_{main} \to 1$) [32,34]. If the bottom encapsulation is prepared by the ultra-thin elastomeric membrane with a Young's modulus lower than human skin (e.g., Ecoflex

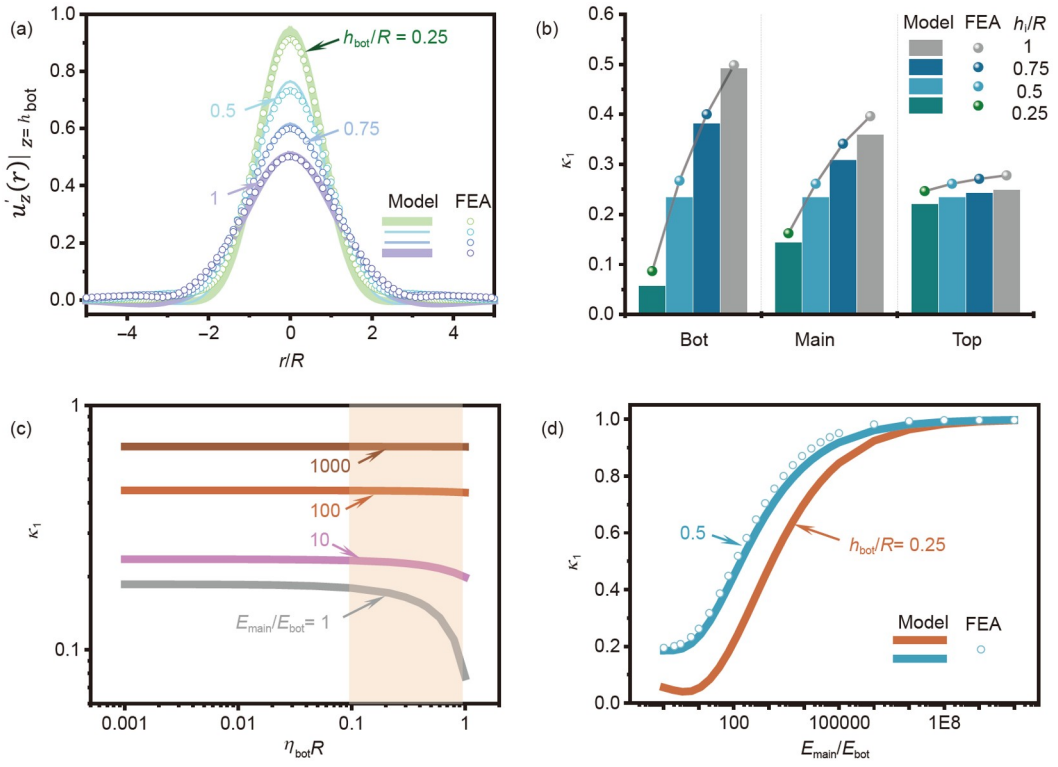

Figure 3 (Color online) (a) Distribution of $u_z'(r)$ at the bottom surface of the main layer for a 3-layer system with different h_{bot}/R (the circle and solid line correspond to FEA and theoretical results, respectively). (b) Strain-isolation effect of bottom encapsulation layer in a three-layer system with a different layer thickness h_i/R (i = top, main and bot, respectively). (c) κ_1 versus $\eta_{bot}R$ for a three-layer system with different Young's modulus. (d) κ_1 versus E_{main}/E_{bot} for a three-layer system with different h_{bot}/R.

Table 2 Parameters of common encapsulating materials for wearable devices

Materials	ρ (g/cm^3)	E (MPa)	v	ρ/E (10^{-4})
PDMS	0.965	0.12–2.8	0.5	3.45–80.4
Ecoflex	1.07	0.055–0.1034	0.47	103.5–194.5
PI	1.39–1.45	2500–3200	0.34	0.004344–0.0058
PET	1.38	1900–3800	0.3–0.4	0.00363–0.00726
PE	0.86–0.96	1070	0.4	0.008037–0.008971
Parylene	1.110	2800	0.4	0.003964

Smooth-on, Silbione 4717, etc.), its $h_{bot}/h_{main} < 0.3$ and $h_{bot}/R < 0.1$ (h_{bot} is about 300 μm and the total thickness of device are more than 1 mm); therefore, the strain-isolation effect in these devices can be neglected (its corresponding κ_1 can less than 1%).

3.2 Stress-isolation effect on external loading

Generally, a loading applied on the top encapsulation layer can be decomposed to the normal and tangential components along the z and r directions, respectively. First, a uniform distributed normal load P_0 with radius R applied on the top encapsulation layer (as shown in Figure 4(a)) is considered. Considering the encapsulation layers are much more compliant than the main layer, the displacements at the bottom of the encapsulation layer can be regarded as zero given the following boundary conditions:

$$\begin{cases} \sigma_z(r,z)\big|_{z=H} = -\sigma_0(|r| \leqslant R), \\ \tau_{rz}(r,z)\big|_{z=H} = 0, \\ u_r(r,z)\big|_{z=0} = 0, \\ u_z(r,z)\big|_{z=0} = 0. \end{cases} \tag{20a}$$

Using the Hankel transform in eq. (S1a), we obtain

$$\begin{cases} \tilde{\sigma}_z(\xi,z)\big|_{z=H} = -\int_0^R \sigma_0 r J_0(\xi r)\mathrm{d}r = -\dfrac{\sigma_0 R}{\xi}J_1(R\xi), \\ \tilde{\tau}_{rz}(\xi,z)\big|_{z=H} = 0, \\ \tilde{u}_r(\xi,z)\big|_{z=0} = 0, \\ \tilde{u}_z(\xi,z)\big|_{z=0} = 0. \end{cases} \tag{20b}$$

Substituting eq. (20a) into eq. (10a) gives

$$\begin{pmatrix} \tilde{\sigma}_z(\xi,z)\big|_{z=0} \\ \tilde{\tau}_{rz}(\xi,z)\big|_{z=0} \\ 0 \\ 0 \end{pmatrix} = C(\xi) \begin{pmatrix} -\dfrac{\sigma_0 R}{\xi}J_1(R\xi) \\ 0 \\ \tilde{u}_r(\xi,z)\big|_{z=H} \\ \tilde{u}_z(\xi,z)\big|_{z=H} \end{pmatrix}. \tag{21}$$

From eq. (21), we obtain

$$\begin{cases}\tilde{\sigma}_z(\xi,z)\big|_{z=0}=\dfrac{C_{13}C_{22}C_{31}-C_{12}C_{23}C_{31}-C_{13}C_{21}C_{32}+C_{11}C_{23}C_{32}+C_{12}C_{21}C_{33}-C_{11}C_{22}C_{33}}{c_{12}c_{21}-c_{11}c_{22}}\tilde{\sigma}_0,\\ \tilde{\tau}_{zr}(\xi,z)\big|_{z=0}=\dfrac{C_{13}C_{22}C_{41}-C_{12}C_{23}C_{41}-C_{13}C_{21}C_{42}+C_{11}C_{23}C_{42}+C_{12}C_{21}C_{43}-C_{11}C_{22}C_{43}}{c_{12}c_{21}-c_{11}c_{22}},\\ \tilde{u}_r(\xi,z)\big|_{z=H}=\dfrac{C_{12}C_{23}-C_{13}C_{22}}{C_{11}C_{22}-C_{12}C_{21}}\tilde{\sigma}_0,\\ \tilde{u}_z(\xi,z)\big|_{z=H}=\dfrac{C_{13}C_{21}-C_{11}C_{23}}{C_{11}C_{22}-C_{12}C_{21}}\tilde{\sigma}_0,\end{cases}\tag{22}$$

where $\boldsymbol{C}_{ij}$ is the elements of the matrix $\mathbf{C}(\xi)$, and $\tilde{\sigma}_0=-\frac{\sigma_0 R}{\xi}J_1(R\xi)$. Based on eqs. (10c) and (22), the displacement and stresses at the interface between the main layer and the top encapsulation layer are governed by

$$\begin{pmatrix}\tilde{\sigma}_z(\xi,z)\big|_{z=H-h_{\text{top}}}\\ \tilde{\tau}_{rz}(\xi,z)\big|_{z=H-h_{\text{top}}}\\ \tilde{u}_r(\xi,z)\big|_{z=H-h_{\text{top}}}\\ \tilde{u}_z(\xi,z)\big|_{z=H-h_{\text{top}}}\end{pmatrix}=\mathbf{C}_{\text{top}}\left(\xi h_{\text{top}}\right)\begin{pmatrix}\tilde{\sigma}_z(\xi,z)\big|_{z=H}\\ \tilde{\tau}_{rz}(\xi,z)\big|_{z=H}\\ \tilde{u}_r(\xi,z)\big|_{z=H}\\ \tilde{u}_z(\xi,z)\big|_{z=H}\end{pmatrix}$$
$$=C_{\text{top}}\left(\xi h_{\text{top}}\right)\begin{pmatrix}-\dfrac{\sigma_0 R}{\xi}J_1(R\xi)\\ 0\\ \dfrac{c_{12}C_{23}-C_{13}C_{22}}{C_{11}C_{22}-C_{12}C_{21}}\\ \dfrac{C_{13}C_{21}-C_{11}C_{23}}{C_{11}C_{22}-C_{12}C_{21}}\end{pmatrix}.\tag{23}$$

Substituting to eq. (23) into the Hankel inverse transform in eq. (S1b), the stress components at the interface between the 2nd-layer and the 3rd-layer are obtained as

$$\sigma_z(r,z)\big|_{z=H-h_{\text{top}}}=\int_0^\infty\tilde{\sigma}_z(\xi,z)\big|_{z=H-h_{\text{top}}}\xi J_0(\xi r)\mathrm{d}\xi,\tag{24a}$$

$$\tau_{rz}(r,z)\big|_{z=H-h_{\text{top}}}=\int_0^\infty\tilde{\tau}_{rz}(\xi,z)\big|_{z=H-h_{\text{top}}}\xi J_1(\xi r)\mathrm{d}\xi.\tag{24b}$$

Here, a stress-isolation index κ_2 is introduced to quantify the protective effect of the top encapsulation layer from normal loading as

$$\kappa_2=1-\mathrm{Max}\left[\frac{\sigma_z(r,z)}{\sigma_0}\bigg|_{z=H-h_{\text{top}}}\right]=1-\frac{\sigma_z(r,z)}{\sigma_0}\bigg|_{r=0,z=H-h_{\text{top}}}.\tag{25}$$

For a three-layered homogeneous media with the same elastic modulus ($E_{\text{top}}=E_{\text{main}}=E_{\text{bot}}=E$, $\nu_{\text{top}}=\nu_{\text{main}}=\nu_{\text{bot}}=\nu$), the solution in eq. (23) simplifies to

$$\tilde{\sigma}_z(\xi,z)=\tilde{\sigma}_0\times\frac{c[\cosh(a\xi)+\xi z\sinh(z\xi)]+(b-2zH\xi^2)\cosh(z\xi)+\xi a\sinh(a\xi)}{b+c\cosh(2H\xi)},\tag{26a}$$

$$\tilde{\tau}_{rz}(\xi,z)=\tilde{\sigma}_0\frac{\xi z[c\cosh(a\xi)+\cosh(z\xi)]-(b-2zH\xi^2-1)\sinh(z\xi)}{b-c\cosh(2H\xi)},\tag{26b}$$

$$\tilde{\sigma}_0=-\frac{\sigma_0 R}{\xi}J_1(R\xi),\tag{26c}$$

where $a=2H-z$, $b=5-12\nu+8\nu^2+2H^2\xi^2$, and $c=3-4\nu$. For the special case of a monolayer system with $H=h_{\text{top}}$, the stress-isolation index further simplifies to

$$\kappa_2=1-4R(1-\nu)\times\int_0^\infty\frac{2(1-\nu)\cosh(H\xi)+H\xi\sinh(H\xi)}{5-12\nu+8\nu^2+2H^2\xi^2+(3-4\nu)\cosh(2H\xi)}\times J_1(R\xi)J_0(\xi r)\mathrm{d}\xi.\tag{27}$$

Using eqs. (24) and (25), the normalized stress components at the top of the main layer and SEI in the pressure sensors after encapsulation can be evaluated to verify that the design protects the sensor and electronics from external loading. Figure 4(b) shows the distribution of the normalized stress component, $\sigma_z(r,z)\big|_{z=H-h_{\text{top}}}/\sigma_0$, at the bottom surface of the top encapsulation layer with different $h'=h_{\text{top}}/R$ under a uniform normal load σ_0. Clearly, the normal stress σ_z/σ_0, at the bottom of the encapsulation layer decreases with increasing layer thickness h' under normal load σ_0, indicating that the SEI of the thicker elastic encapsulation layer is more prominent. For the case of an encapsulation pressure sensor on a wearable device, 18% of the normal stress from the external load will be shielded when the size of the external load (R) is close to the thickness of the encapsulation layer (h) (i.e., h_{top}/R close to 1). Moreover, the normal load at the top of the encapsulation layer induces extra shear stress at the bottom (the interface between sensor and encapsulation layer), and its maximum occurs at the edge of the load ($r=R$) (Figure S2, Supporting Information online). In some cases, particularly for piezoelectric (PZT) sensors, the induced shear stress along the layer interface can increase the tensile stress in a super-sensitive PZT sensor, therefore improving its sensitivity.

In addition to the thickness, the elastic modulus of layers also affects the SEI. Figure 4(c) shows the distribution of the

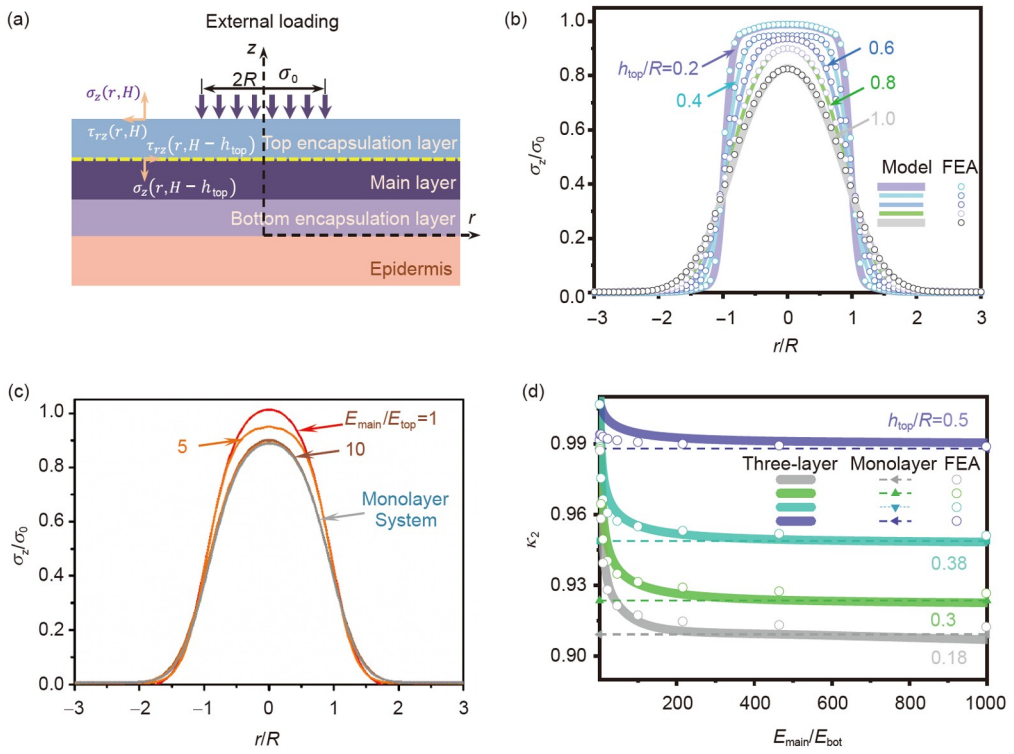

Figure 4 (Color online) (a) Schematic illustration of stress-isolation effect in a three-layer encapsulation system. (b) Distribution of $\sigma_z(r,z)\big|_{z=H-h_{top}}/\sigma_0$ at the top surface of the main layer for a three-layer system with different h_{top}/R (the circle and solid line correspond to the finite-element analysis (FEA) and theoretical results, respectively). (c) Distribution of $\sigma_z(r,z)\big|_{z=H-h_{top}}/\sigma_0$ for three-layer system with different Young's modulus. (d) κ_2 versus E_{main}/E_{bot} for a three-layer system with different h_{top}/R. Noted that the circle and solid line correspond to the theoretical results and FEA, respectively.

normalized stress σ_z/σ_0 on the top of the 2nd-layer for different Young's modulus (E_{main}/E_{top} = 1, 5 and 10), the maximum of σ_z/σ_0 exibits a slightly decreasing tendency (decreases from 1 to 0.9) when E_{main}/E_{top} increases one order of magnitude from 1 to 10. Figure 4(d) shows κ_2 versus E_{main}/E_{top} for different top encapsulation thicknesses (h_{top}/R = 0.18, 0.3, 0.38, 0.5). It is clear that κ_2 approaches a contant value, which could be estimated by the monolayer system (eq. (27)), when the main layer is very rigid as compared with the top encapsulation layer (e.g., $E_{main}/E_{top}=10^3$).

Similarly, the stress-isolation analysis of encapsulated device for a tangential load is given in Appendix C. The tangential load at the top encapsulation layer also causes additional normal stresses at the top surface of the main layer, and its corresponding maximum or minimum value occurs at the edge (r = 0) or center of the load (r = R), as shown in Figure S3(b).

FEA was performed to verify the results from the proposed analytic model. Theoretical results are in good agreement with FEA ones, as shown in Figures 3(b) and 4(b)

4 Conclusion

In summary, we developed an analytic model for evaluating the strain- and stress-isolation effects in wearable devices. The soft, elastomeric encapsulation layers and electronic main layer are modeled as transversely isotropic mediums, and two isolation indexes that quantify the strain- and stress-isolation effects are proposed. The results show that the strain- and stress-isolation effects strongly depend on the thickness, density, and elastic modulus of both the encapsulation layers and the main layer. Incorporating the theory described, we can further optimize the top and bottom elastomeric encapsulation layers and the structure of electronic components to achieve a high sensitivity while protecting the wearable devices from external forces.

This work was supported by the National Natural Science Foundation of China (Grant Nos. 12172319, 11872326, and 12072057), the Natural Science Foundation of Hunan Province (Grant Nos. 2021JJ30648, and 2021JJ30641), the Furong Scholars Programme of Hunan Province, the LiaoNing Revitalization Talents Program (Grant No. XLYC2007196), the Fundamental Research Funds for the Central Universities (Grant No. DUT20RC(3)032), the National Science Foundation Graduate Research

Fellowship (Grant No. 1842165) and the Ford Foundation Predoctoral Fellowship.

Supporting Information

The supporting information is available online at tech.scichina.com and link.springer.com. The supporting materials are published as submitted, without typesetting or editing. The responsibility for scientific accuracy and content remains entirely with the authors.

1 Han Z, Cheng Z, Chen Y, et al. Fabrication of highly pressure-sensitive, hydrophobic, and flexible 3D carbon nanofiber networks by electrospinning for human physiological signal monitoring. Nanoscale, 2019, 11: 5942–5950
2 Liu Y, Fan H, Li K, et al. Strain-isolation bridge structure to improve stretchability of highly sensitive strain sensors. Adv Mater Technol, 2019, 4: 1900309
3 Hao D P, Yang R X, Yi N, et al. Highly sensitive piezoresistive pressure sensors based on laser-induced graphene with molybdenum disulfide nanoparticles. Sci China Tech Sci, 2021, 64: 2408–2414
4 Zhao R, Yang H, Nie B Q, et al. Highly transparent, antifreezing and stretchable conductive organohydrogels for strain and pressure sensors. Sci China Tech Sci, 2021, 64: 2532–2540
5 Wang C, Cai M, Hao Z, et al. Stretchable, multifunctional epidermal sensor patch for surface electromyography and strain measurements. Adv Intelligent Syst, 2021, 3: 2100031
6 Ershad F, Thukral A, Yue J, et al. Ultra-conformal drawn-on-skin electronics for multifunctional motion artifact-free sensing and point-of-care treatment. Nat Commun, 2020, 11: 1–3
7 Cheng X, Zhang F, Bo R, et al. An anti-fatigue design strategy for 3D ribbon-shaped flexible electronics. Adv Mater, 2021, 33: 2102684
8 Zhou H, Zhang Y, Qiu Y, et al. Stretchable piezoelectric energy harvesters and self-powered sensors for wearable and implantable devices. Biosens Bioelectron, 2020, 168: 112569
9 Park Y, Franz C K, Ryu H, et al. Three-dimensional, multifunctional neural interfaces for cortical spheroids and engineered assembloids. Sci Adv, 2021, 7: eabf9153
10 Grajales-Reyes J G, Copits B A, Lie F, et al. Surgical implantation of wireless, battery-free optoelectronic epidural implants for optogenetic manipulation of spinal cord circuits in mice. Nat Protoc, 2021, 16: 3072–3088
11 Reeder J T, Choi J, Xue Y, et al. Waterproof, electronics-enabled, epidermal microfluidic devices for sweat collection, biomarker analysis, and thermography in aquatic settings. Sci Adv, 2019, 5: eaau6356
12 Li H, Ma Y, Huang Y. Material innovation and mechanics design for substrates and encapsulation of flexible electronics: A review. Mater Horiz, 2021, 8: 383–400
13 Wang X, Liu Y, Cheng H, et al. Surface wettability for skin-interfaced sensors and devices. Adv Funct Mater, 2022, 32: 2200260
14 Zhang Y, Chen Y, Huang J, et al. Skin-interfaced microfluidic devices with one-opening chambers and hydrophobic valves for sweat collection and analysis. Lab Chip, 2020, 20: 2635–2645
15 Liu Y, Cheng M, Huang J, et al. Strain-tunable microfluidic devices with crack and wrinkle microvalves for microsphere screening and fluidic logic gates. ACS Appl Mater Interfaces, 2021, 13: 36849–36858
16 Wang X, Ma Y, Xue Y, et al. Collapse of liquid-overfilled strain-isolation substrates in wearable electronics. Int J Solids Struct, 2017, 117: 137–142
17 Wu J, Li M, Chen W Q, et al. A strain-isolation design for stretchable electronics. Acta Mech Sin, 2010, 26: 881–888
18 Xu R, Zhang K, Xu X, et al. Superhydrophobic WS_2-nanosheet-wrapped sponges for underwater detection of tiny vibration. Adv Sci, 2018, 5: 1700655
19 Ruth S R A, Feig V R, Tran H, et al. Microengineering pressure sensor active layers for improved performance. Adv Funct Mater, 2020, 30: 2003491
20 Sun J Y, Lu N, Yoon J, et al. Inorganic islands on a highly stretchable polyimide substrate. J Mater Res, 2009, 24: 3338–3342
21 Ma Y, Pharr M, Wang L, et al. Soft elastomers with ionic liquid-filled cavities as strain isolating substrates for wearable electronics. Small, 2017, 13: 1602954
22 Xu S, Zhang Y, Jia L, et al. Soft microfluidic assemblies of sensors, circuits, and radios for the skin. Science, 2014, 344: 70–74
23 Fan J A, Yeo W H, Su Y, et al. Fractal design concepts for stretchable electronics. Nat Commun, 2014, 5: 3266
24 Wang J, Fang S, Chen L. The state vector methods for space axisymmetric problems in multilayered piezoelectric media. Int J Solids Struct, 2002, 39: 3959–3970
25 Yang Z, Zheren W, Dazhi G. The transfer matrix method for solving axisymmetrical problems in mutilayered elastic half space. China Civil Eng J, 1992, 25: 37–43
26 Yang Z, Zhang Y S. Explicit solution for axisymmetrical multilayered elastic half space problems by exact stiffness matrix method. Chin Quart Mech, 2003, 24: 395–400
27 Pestel E, Leckie F A. Matrix Methods in Elastomechanics. New York: McGraw-Hill, 1963
28 Chen Y, Liu F, Lu B, et al. Skin-like hybrid integrated circuits conformal to face for continuous respiratory monitoring. Adv Electron Mater, 2020, 6: 2000145
29 Khan S M, Qaiser N, Shaikh S F, et al. Design analysis and human tests of foil-based wheezing monitoring system for asthma detection. IEEE Trans Electron Devices, 2019, 67: 249–257
30 Shi X, Wang H, Xie X, et al. Bioinspired ultrasensitive and stretchable mxene-based strain sensor via nacre-mimetic microscale "brick-and-mortar" architecture. ACS Nano, 2018, 13: 649–659
31 Liu Y, Sheng Z, Huang J, et al. Moisture-resistant MXene-sodium alginate sponges with sustained superhydrophobicity for monitoring human activities. Chem Eng J, 2022, 432: 134370
32 Lee K H, Ni X, Lee J Y, et al. Mechano-acoustic sensing of physiological processes and body motions via a soft wireless device placed at the suprasternal notch. Nat Biomed Eng, 2020, 4: 148–158
33 Zhai W, Wang C, Wang S, et al. Ultra-stretchable and multifunctional wearable electronics for superior electromagnetic interference shielding, electrical therapy and biomotion monitoring. J Mater Chem A, 2021, 9: 7238–7247
34 Jeong H, Lee J Y, Lee K H, et al. Differential cardiopulmonary monitoring system for artifact-canceled physiological tracking of athletes, workers, and COVID-19 patients. Sci Adv, 2021, 7: eabg3092
35 Xue Z, Song H, Rogers J A, et al. Mechanically-guided structural designs in stretchable inorganic electronics. Adv Mater, 2019, 32: 1902254
36 Zhao J, Zhang F, Guo X, et al. Torsional deformation dominated buckling of serpentine structures to form three-dimensional architectures with ultra-low rigidity. J Mech Phys Solids, 2021, 155: 104568
37 Li M, Li X, Che L X, et al. Non-uniform global-buckling and local-folding in thin film of stretchable electronics. Int J Mech Sci, 2020, 175: 105537
38 Li K, Cheng X, Zhu F, et al. A generic soft encapsulation strategy for stretchable electronics. Adv Funct Mater, 2019, 29: 1806630